

# Urban pollution monitoring with the AOTF-based NO<sub>2</sub> camera: validation with other DOAS instruments

Pierre Gramme<sup>1,\*</sup>, Cedric Busschots<sup>1,\*</sup>, Emmanuel Dekemper<sup>1,\*</sup>, Didier Pieroux<sup>1</sup>, Noel Baker<sup>1</sup>, Stefano Casadio<sup>2</sup>, Anna Maria Iannarelli<sup>2</sup>, Nicola Ferrante<sup>2</sup>, Annalisa Di Bernardino<sup>3</sup>, Paolo Pettinari<sup>4</sup>, Elisa Castelli<sup>4</sup>, Luca Di Liberto<sup>5</sup>, and Francesco Cairo<sup>5</sup>

<sup>1</sup>Royal Belgian Institute for Space Aeronomy, Ringlaan 3, 1180 Ukkel, Belgium

<sup>2</sup>Serco Italia S.p.A., Via Bernardino Alimena 111-119, 00173 Rome, Italy

<sup>3</sup>Sapienza University of Rome, Physics Department, Piazzale A. Moro 5, 00185 Rome, Italy

<sup>4</sup>National Research Council (CNR), Institute of Atmospheric Sciences and Climate (ISAC), Via Piero Gobetti 101, 40129 Bologna, Italy

<sup>5</sup>National Research Council (CNR), Institute of Atmospheric Sciences and Climate (ISAC), Via Fosso del Cavaliere 100, 00133 Rome, Italy

\*These authors contributed equally to this work.

**Correspondence:** Pierre Gramme (pierre.gramme@aeronomie.be) and Cedric Busschots (cedric.busschots@aeronomie.be)

**Abstract.** Elevated surface concentrations of nitrogen dioxide (NO<sub>2</sub>) are associated with poor air quality, making its detection and monitoring important for human health and the environment. Existing instruments such as the TROPOMI satellite currently deliver daily global maps of NO<sub>2</sub> tropospheric columns, and the future Sentinel-4 instrument will return hourly maps. While areas of strong concentrations (cities, large industries) can be detected in these satellite observations, their spatio-temporal resolution remains too coarse to capture local hot spots and quick variations.

In the context of urban air quality monitoring, we present a new type of remote sensing instrument capable of observing spatial and temporal gradients in the NO<sub>2</sub> field which is not currently possible with either space instruments or from the routine operations of conventional diffraction grating and other ground-based remote sensing instruments. This novel instrument is based on an acousto-optical tunable filter (AOTF) located at the heart of a telecentric imaging system. The instrument acquires spectral images in the region 430–455 nm, where NO<sub>2</sub> exhibits strong absorption features. A dense spectral sampling was commanded in order to enable the application of the DOAS method (differential optical absorption spectroscopy) in the processing of the spectra measured by each detector pixel.

In March 2024, the instrument was deployed at the BAQUNIN supersite for atmospheric research, located in the center of Rome. In order to validate the NO<sub>2</sub> camera measurements, coincident acquisitions by a MAX-DOAS and a Pandora spectrometer were performed. The results show very good agreement among the three instruments. They also illustrate the additional capabilities of the NO<sub>2</sub> camera in observing the spatial and temporal variability of the urban NO<sub>2</sub> field.

## 1 Introduction

Humans are directly exposed to the chemical composition of Earth's boundary layer, the lowest part of the troposphere where emissions from the surface are mixing. In that layer, the nitrogen oxides ( $\text{NO}_x$ ) family is made of nitrogen oxide ( $\text{NO}$ ) and nitrogen dioxide ( $\text{NO}_2$ ), the former being primarily released in combustion processes (both natural or anthropogenic) while the latter is produced by reaction of  $\text{NO}$  with ozone ( $\text{O}_3$ ) or hydroperoxy radical ( $\text{HO}_2$ ). Through photolysis,  $\text{NO}_2$  can be converted back into  $\text{NO}$ , such that a photochemical equilibrium persists most of the day. Among other effects, high levels of  $\text{NO}_x$  are associated with poor air quality, given the role of the molecule in the advent of photochemical smog episodes (Seinfeld and Pandis, 2006).

Of these  $\text{NO}_x$  compounds, nitrogen dioxide ( $\text{NO}_2$ ) is the most important for human health (World Health Organization, 2021). There is scientific evidence that chronic exposure to  $\text{NO}_2$  can cause emphysema (Last et al., 1994) and that, together with ozone, it increases oxidative stress in the small airways within the lungs (Morrow, 1984). Long-term exposure to ambient  $\text{NO}_2$  is found to be correlated with increased mortality (Chen et al., 2024; Huangfu and Atkinson, 2020).

This negative influence on human health prompted the World Health Organization (WHO) to release Air Quality Guidelines, updated in 2021, and more recently translated into a European law (Directive 2022/0347). While European Union Member States are required to deploy air sampling stations, with some guidelines on the number of stations and their location, the Directive fails to address the problem of the large variation of exposure by citizens living in different neighborhoods of close proximity. Such large differences have been observed in citizen science projects, such as the *CurieuzenAir/CurieuzeNeuzen* experiment, in which thousands of sampling flasks have been deployed in both Brussels (Lauriks et al., 2022) and Flanders (De Craemer et al., 2020). The WHO identifies this inadequate monitoring of spatial variations in the concentration of pollutants such as  $\text{NO}_2$  as one of the main gaps in the global coverage of air pollution monitoring (World Health Organization, 2021). These spatial and temporal differences are especially pronounced in urban environments.

In recent years, several new remote sensing instruments have been developed that attempt to capture this variability of the  $\text{NO}_2$  field with a high spatial and temporal resolution. These instruments work in the UV-visible wavelength range, where  $\text{NO}_2$  is a strong absorber. Many consisted in grating instruments, whose field of view is steered mechanically (Manago et al., 2018; Peters et al., 2019; Mettepenningen et al., 2024). Retaining all the strengths of the differential optical absorption spectroscopy (DOAS) technique (Platt and Stutz, 2008), the images are constructed slice by slice, which is subject to artifacts in case of a dynamic scene. One prototype of a native  $\text{NO}_2$  imaging instrument relied on the gas correlation technique (Kuhn et al., 2022) but was only tested on large point source plumes. Another concept studied the potential of a Fabry-Pérot interferometer-based polychromatic imaging system for atmospheric trace gases remote sensing, including  $\text{NO}_2$ , with an elaborated use of the periodic structures of the species cross sections (Kuhn et al., 2019); to our knowledge, no real-world application of this concept to the measurement of  $\text{NO}_2$  has been realized yet.

An acousto-optical tunable filter (AOTF)-based instrument produced high spatio-temporal maps of  $\text{NO}_2$  in the plume released by a thermal power plant (Dekemper et al., 2016). While the concept requires sweeping over wavelengths, it is a native

50 imaging system with relatively high spatial resolution compared to other techniques. This paper discusses the improvements made to this instrument, and demonstrates its capability to make quantitative measurements of the NO<sub>2</sub> field.

## 2 The improved AOTF-based NO<sub>2</sub> camera

The AOTF-based NO<sub>2</sub> camera concept stems from the ALTIUS instrument, an ESA satellite mission for the monitoring of the stratospheric O<sub>3</sub> layer which relies on the acquisition of spectral images of the atmospheric limb at selected wavelengths  
55 (Fussen et al., 2019). As part of the ALTIUS mission pre-developments, a proof-of-concept optical breadboard of its VIS channel was produced and tested in the laboratory. Although not meant to leave the laboratory, its potential for imaging NO<sub>2</sub> plumes was recognized and tested during the AROMAT-II campaign (Merlaud et al., 2020). That version of the instrument as well as the results of the campaign were fully described in (Dekemper et al., 2016).

The instrument being reported here is an improved version of the original breadboard in almost every aspect, from basic pa-  
60 rameters such as reduced size and mass, to its improved optical performance and acquisition software (see Section 2.1). Its raw data remain monochromatic images stacked in hypercubes. During the AROMAT campaign operations, only four wavelengths were acquired. In Rome, routine operations included wavelengths between 427 and 454.9 nm, sampled every 0.15 nm. Further details of the wavelength sampling are described later in Section 4. This allows to apply a DOAS algorithm and achieve higher accuracy.

65 In Section 2.1, we describe the instrument, its operating scheme, and the raw data it produces. Sections 2.2 and 2.3 discuss the spectral response function of the instrument and the data acquisition respectively. Then, in Section 2.4, we discuss the main differences between this instrument and the conventional diffraction grating-based spectrometers which are currently used to monitor the field of NO<sub>2</sub> as part of operational networks.

### 2.1 Instrument description

70 The fundamental instrumental concept described in (Dekemper et al., 2012) and (Dekemper et al., 2016) has been kept: a telecentric front-end module captures the light and sends it on to the AOTF. Upon crossing the crystal, a narrow band of the incident light spectrum experiences a coupling with the acoustic beam created in the crystal by a piezo-electric transducer. The acousto-optic interaction diffracts the selected part of the spectrum into another direction, such that two beams leave the AOTF: one containing photons of the same energy (the monochromatic beam), and the other containing the rest of the  
75 spectrum (the white beam). The back-end optics only captures the diffracted beam, which forms the monochromatic image on the detector. The selection of another wavelength happens by tuning the acoustic wave frequency. Fig. 1 shows a picture of the optomechanical system. The fundamental physics of acousto-optic interaction in birefringent crystals is described in (Harris and Wallace, 1969; Chang, 1974). Further details on telecentric systems using AOTFs can be found in, e.g. (Suhre et al., 2004), and a discussion on the optimization of AOTF parameters used for spectral imaging applications is provided in (Voloshinov  
80 et al., 2007).

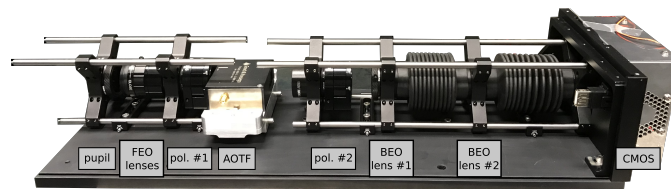


**Figure 1.** The current optics setup is made with commercial off-the-shelf components.



**Figure 2.** The NO<sub>2</sub> camera and the two reference instruments installed for the campaign at the BAQUNIN-APL supersite.

One of the most significant improvements concerns the field of view (FOV) which was increased to  $23^\circ \times 23^\circ$  by reducing the focal length of the telecentric lens. The size of the back-end optics was also reduced by using shorter focal lengths. As a consequence, the instrument is now much more compact (see Table 1) and can be manipulated by a single person. The electronics (radio frequency (RF) generation and amplification, single-board computer) fit in a separate box. For the validation campaign, a pan-and-tilt head was used to control the pointing of the instrument (EKO sun tracker with GPS receiver). The optics, electronics, and pointing modules have all been placed on a tripod. The camera housing was redesigned to withstand adverse weather; the optics are sealed off from the outside, while the cooled detector is partially outside this sealed environment, so that fresh air can reach the cooling block of the Peltier element. Fig. 2 shows the exterior of the camera and its surrounding environment during the campaign.

90 Table 1 details the specifications of the original versus the newer version of the NO<sub>2</sub> camera.

The software reliability was tackled with newly designed control software that runs on an ARM-based single board computer. An OKdo Rock 5B with 8GB RAM was selected for this purpose. It accepts an NVMe M.2 SSD to temporarily store the acquired images. It is responsible for the synchronized operation of the detector, RF electronics, and EKO. At night, the raw measurement data are transferred automatically to storage servers over the internet.

## 95 2.2 Spectral response function

The instrument's spectral response function (SRF) is approximated by a variable-width Gaussian convolution scheme, where the full width at half maximum (FWHM) of the kernel evolves as a function of the central wavelength, as shown in Table 2. These choices were made from fitting the convolved theoretical solar spectrum (Chance and Kurucz, 2010) to the measured

**Table 1.** Comparison of the original and current versions of the NO<sub>2</sub> camera.

	Original (Dekemper et al., 2016)	This work
Size of optics channel	1 m	40 cm
Mass	40 kg	6 kg
FoV	$5.8^\circ \times 5.8^\circ$	$23^\circ \times 23^\circ$
AOTF	Gooch & Housego model TF625-350-2-12-BR1A	Gooch & Housego model TF625-350-2-12-BR1A
Spectral range	at most 430 – 450 nm	at most 400 – 490 nm
Detector	Princeton Instrument Pixis 512B CCD	ZWO ASI2600MM Pro CMOS
ADC	16 bits	16 bits
Read noise	$5 e^-$ rms	$<1.4 e^-$ rms
# pixels	512x512	6248x4176 (binned to 512x512)
Pixel area	$24 \times 24 \mu\text{m}^2$	$3.76 \times 3.76 \mu\text{m}^2$ (binned to $30 \times 30 \mu\text{m}^2$ )
Per-pixel FoV	$0.011^\circ \times 0.011^\circ$	$0.045^\circ \times 0.045^\circ$ (binned)
Full well	$3 \cdot 10^5 e^-$	$5 \cdot 10^4 e^-$ (binned to $3.2 \cdot 10^6 e^-$ )
Pointing control	elevation (manual)	azimuth and elevation with EKO STR-21G

**Table 2.** Instrument’s spectral resolution (width of Gaussian kernel) as a function of the wavelength. A linear interpolation is performed between the values shown here.

Central wavelength	400 nm	430 nm	460 nm	490 nm
FWHM	1.0 nm	1.1 nm	1.7 nm	2.5 nm

intensity at zenith during a calibration experiment. The merit function for the fit was the mean absolute difference between  
100 both spectra, after taking their logarithm and subtracting a low-order polynomial approximation from each.

### 2.3 Data acquisition

The image projected on the CMOS detector is roughly square. Of the full rectangular native resolution of 6248×4176 pixels,  
only a square region of interest of 4096 by 4096 pixels is selected. The resulting image is then binned in two steps. A first  
4×4 binning is executed by the detector itself, then the software bins the image again, leading to a final resolution of 512 by  
105 512 pixels. The main motivation for binning is the increase of the signal-to-noise ratio (SNR) by a factor 8. This is required  
given the target variability of about 1% to be detected in the signal intensity while keeping the per-frame exposure time at  
1000 ms. As positive side-effects, the frame rate is also increased, and the data storage needs are reduced. The gain parameter  
was chosen to be high enough to minimize the read noise and quantization noise and low enough to avoid saturation.

The wavelength band that is sampled for the NO<sub>2</sub> measurements ranges from 427 to 454.9 nm, focusing on the strong  
110 spectral features of NO<sub>2</sub>. Every 0.15 nm an image is taken. This sampling ensures compliance with the Nyquist criterion, as

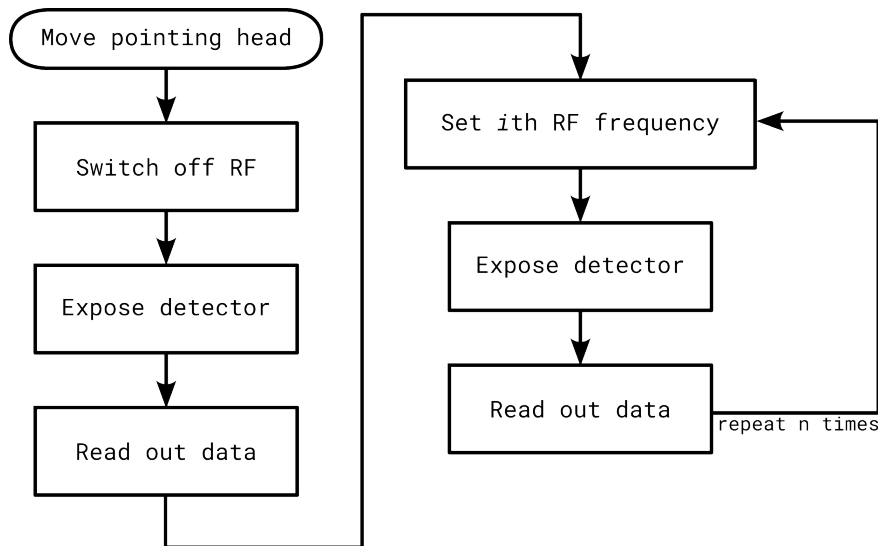


**Figure 3.** Schematic representation of the acquisition process for a single *hypercube*. For every acoustic frequency  $n$ , the corresponding RF frequency  $i$  needs to be set.

the spectral resolution of the filter is not smaller than 0.7 nm, expressed as the FWHM of the SRF. In total, this amounts to 188 distinct spectral images forming a hyperspectral cube (or simply a cube). An additional image is acquired at the start of every cube. This image is taken with the AOTF off (0 W of RF power injected into the transducer), which therefore only contains the instrument stray light. In the data processing, this stray light image can be used to remove the stray light from all the other spectral images. Each of the images includes metadata about the scene location, time, and camera and pointing parameters.

During a complete acquisition, the instrument is first pointed in the direction of the scene of interest using the EKO. Then, one or multiple cubes of the scene are acquired, followed by a cube acquired while the instrument points at the zenith. These zenith cubes are needed to remove the solar spectrum and the stratospheric signal during the data analysis. A flow chart of the complete acquisition scheme is shown in Fig. 3.

## 2.4 Main differences with grating-based instruments

The goal of the NO<sub>2</sub> camera is to go a step further in terms of the observing capability of the small-scale spatial structures and the high temporal variability of the NO<sub>2</sub> field emanating from distributed sources of a city. These new observing capabilities should be assessed with respect to the performance of operational remote sensing instruments, such as the MAX-DOAS instruments of the Network for the Detection of Atmospheric Composition Change (NDACC) research infrastructure (Van Roozendaal et al., 2024), or the Pandora spectrometers of the Pandonia Global Network (Herman et al., 2009).

The MAX-DOAS and the Pandora instruments are diffraction grating spectrometers that measure the UV-VIS solar light which is either scattered by the atmosphere or directly transmitted. The former method yields more freedom with respect to the observation directions, as potentially any pair of azimuth and elevation angle can be targeted. Some instrument designs can

also sample a range of azimuth or elevation angles in one single acquisition (e.g., see Peters et al. (2019)). In that case, a 1-D  
130 array of NO<sub>2</sub> slant columns can be retrieved in one single acquisition. When an image of a scene is desirable, this method can  
be expanded to two dimensions by sweeping the 1-D field of view along the second dimension of the scene (Lohberger et al.,  
2004; Heue et al., 2008; Peters et al., 2019; Mettepenningen et al., 2024). However, a limitation of this method is the loss of  
temporal consistency between the different slices of the scene, especially when observing dynamic features such as plumes  
(Platt et al., 2014).

135 The NO<sub>2</sub> camera uses a different method to create images of the NO<sub>2</sub> field. Instead of scanning the scene, Dekemper  
et al. (2016) proposed to capture complete images of the scene, but one wavelength at a time. The imaging quality is that of  
a real imaging system, offering a higher spatial sampling than fiber-bundled based diffraction grating spectrometers, while  
temporal variations can still be tracked in successive images. One drawback lies in the perturbations caused by the spectra  
recorded by pixels which have seen objects moving during the cube acquisitions. Additionally, the optical throughput of a  
140 telecentric AOTF-based imager is lower than that of a diffraction grating spectrometer, yielding a lower SNR. This lower SNR  
allows observations with SZA up to 90° while maintaining the per-frame exposure at 1 second, but twilight observations would  
require adaptations.

On the other hand, this method has the advantage that images are acquired from the start. Pointing errors are easily corrected  
by using features in the pictures. More importantly, highly dynamic processes can be detected and monitored, especially when  
145 the camera is focusing on a limited number of wavelengths. Whereas diffraction grating-based systems automatically record the  
complete spectrum for their design bandwidth, AOTF-based systems allow the user to cherry-pick the wavelengths of interest:  
there is no fixed sequence of wavelengths required. Therefore, a wavelength band of interest can be defined for any species, and  
only this wavelength band will be sampled by the camera. In the context of satellite retrievals, Ruiz Villena et al. (2020) proved  
the feasibility of discrete-wavelength DOAS using only 10 carefully chosen wavelengths and reaching correlations above 99 %  
150 with the operational products from OMI and TROPOMI. The power plant campaign described by Dekemper et al. (2016)  
follows a slightly different approach based on 8 wavelengths. This way, the number of images required can be decreased,  
bringing the time for a single scene measurement below 10 seconds.

### 3 NO<sub>2</sub> camera data processing

#### 3.1 Overview

155 The data processing for the NO<sub>2</sub> camera is organized into Level-0 (raw spectra), Level-1 (calibrated spectra) and Level-2  
(retrieval outcome). The main processing steps are shown in Fig. 4, and more details are provided in the next sections.

#### 3.2 Level-1 Processor

The first step of the Level-1 processor (L1P) is to convert the acquired raw data from digital number to electron count. A  
preliminary calibration experiment was performed in order to compute a photon transfer curve (PTC) and derive its parameters,

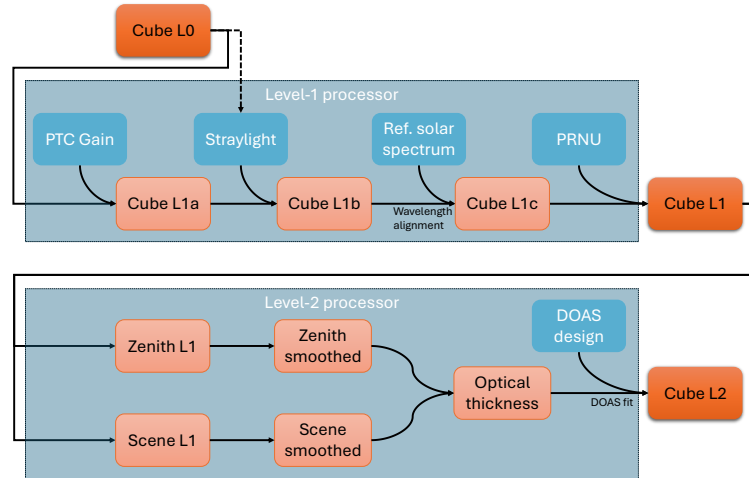


**Figure 4.** Overview of the data processing for the retrieval of NO<sub>2</sub> dSCDs (Level-2 data) from the NO<sub>2</sub> camera acquisitions (Level-0 data).

160 following Janesick (2007). At gain parameter 200 ( $\times 0.1$  dB), used during the campaign, our computations gave a gain of  $0.0793 e^-/DN$ , a read noise of  $1.206 e^-$ , and a fixed pattern noise (FPN) of 0.2%, confirming the vendor characteristics. The PTC showed that the CMOS detector's response is very close to linear, so that the conversion to electrons amounts to a simple multiplication by the gain (and a detector offset which can be ignored thanks to the following stray light removal). The stray light images (acquired at least once per hyperspectral cube) are also converted to electrons ( $e^-$ ), and subtracted pixel by pixel  
 165 from the target images. To maintain physical interpretability, all values under  $1 e^-$  are forced to  $1 e^-$  (i.e. close to the read noise).

An illustration of this stray light removal is shown in Fig. 5. The intensity of stray light observed is typically less than 10% of the scene intensity, except in a small region of about  $70 \times 70$  pixels. This region changes slightly depending on pointing and solar angles, and its stray light may reach values comparable to the real stray light-corrected intensity (especially on scenes  
 170 with less light in their lower part, and at wavelengths under 435 nm).

The optical wavelength filtered by the AOTF at a given acoustic frequency is known to depend on the crystal temperature, varying by about 0.1 nm per K. Although this variation can be computed and corrected for, a more precise wavelength registration is obtained by detecting the Fraunhofer lines, which are clearly visible in the measured spectra. For this purpose, the average intensity at the  $64 \times 64$  central pixels of the cube is compared to the convolved solar reference spectrum, same as  
 175 in Section 2.2. The wavelength correction function is the solution of a non-linear optimization problem whose search space consists of all increasing affine functions of the wavelength, with the identity function as the start point. The score which is minimized is the mean absolute difference of logarithms, after subtracting broadband differences as in Section 2.2.

The final step in Level-1 processing is to correct for pixel response non-uniformity (PRNU), a type of instrumental bias where some pixels would show a different sensitivity from others when exposed to the same input signal. Because this PTC

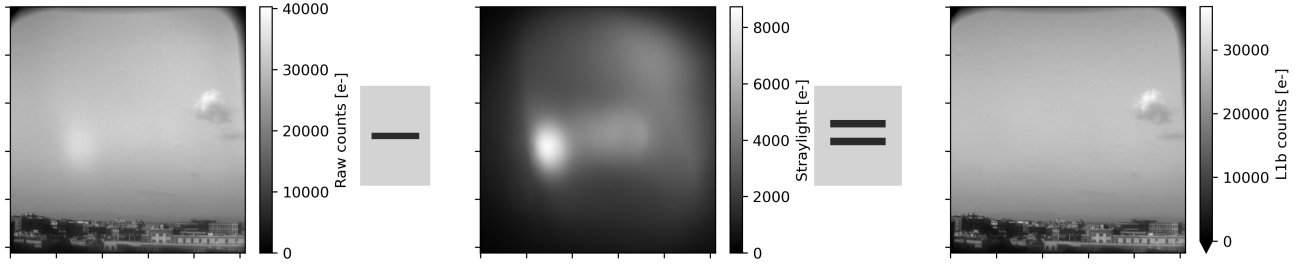


**Figure 5.** Illustration of stray light removal. Note the smaller values in the color scale for the central image, which was captured with the AOTF turned off.

180 analysis showed no significant non-linearity in the instrument’s response, we could use the PTC data to model the PRNU with a simple per-pixel scaling factor independent of the wavelength and of light intensity, even though these hypotheses may not be fully correct. This scaling factor is computed on one reference zenith cube, typically the same as used in Level-2 data processing, taking the per-pixel average intensity across all wavelengths. Note that the first step of Level-2 data processing (see below) is to compute the ratio between the zenith and scene intensities. Therefore, regardless of the choice of linear scaling  
 185 used in the PRNU correction, it will not have any impact on the Level-2 product. That correction can thus be considered as a cosmetic step, only useful when displaying Level-1 images.

Putting it all together, the Level-1 intensity in electrons  $I_{L1}$  at wavelength  $\lambda$  and pixel  $i, j$  is computed as:

$$I_{L1}(\lambda, i, j) = \frac{\max\left(1, G S(\tilde{\lambda}, i, j) - G S_0(i, j)\right)}{\text{PRNU}(i, j)}, \quad (1)$$

190 where

- $\tilde{\lambda}$  is the nominal wavelength, before alignment;
- $\lambda$  is the truly measured wavelength after alignment:  $\lambda = \tilde{\lambda} + \Delta(\tilde{\lambda})$ , where  $\Delta$  is a smooth function of the nominal wavelength optimizing the alignment of Fraunhofer structure;
- $G$  is the detector’s gain;
- 195 –  $S$  is the L0 signal intensity in digital numbers;
- $S_0$  is the L0 stray light signal intensity in digital numbers (i.e. with AOTF off);
- $I_{L1}$  is the Level-1 signal intensity in electrons;
- $\text{PRNU}(i, j)$  is the PRNU factor.

In addition to the calibrated light intensity, a pointing map is computed as well, assigning an elevation and azimuth viewing  
 200 angle to each pixel of the Level-1 image. This map is calibrated using prominent features, such as buildings and mountains, whose viewing angles were determined from publicly available topographic maps and/or aerial photos. Its precision is expected around  $0.05^\circ$  (one pixel).

### 3.3 Level-2 Processor

The retrieval of NO<sub>2</sub> differential slant column densities (dSCDs) from hyperspectral cubes is based on the well established  
 205 DOAS method (Differential Optical Absorption Spectroscopy, see (Platt and Stutz, 2008)), which relies on the Beer–Lambert  
 law:

$$I(\lambda) = I_0(\lambda) \cdot \exp\left(-\sum_{k=1}^K S^k(\lambda)c_k\right), \quad (2)$$

where

- $I(\lambda)$  is the measured spectrum of interest, after extinction in the atmosphere,
- 210 –  $I_0(\lambda)$  is the zenith spectrum, an approximation of the spectrum at the top of the atmosphere,
- $S^k(\lambda)$  is the absorption cross-section of the species  $k$ , depending on wavelength [cm<sup>2</sup>/molec],
- $c_k$  is the dSCD of the species  $k$  [molec/cm<sup>2</sup>].

The principle of the DOAS method is to focus on high-frequency spectral structures in this equation, approximating the low-  
 frequency structures (such as instrumental effects, aerosol scattering, etc.) with a low-order polynomial  $P_{\leq n}(\lambda) = \sum_k p_k \lambda^k$ .  
 215 Defining the optical thickness  $\tau(\lambda)$  as the log-ratio, the previous equation becomes:

$$\tau(\lambda) \equiv \log \frac{I_0(\lambda)}{I(\lambda)} = \sum_{k=0}^n p_k \lambda^k + \sum_{k=1}^K S^k(\lambda)c_k. \quad (3)$$

Writing  $\{\lambda_l\}_{l=1\dots L}$  for the wavelengths at which the optical thickness was measured, and defining the DOAS design matrix as

$$A \equiv \begin{pmatrix} 1 & \lambda_1 & \cdots & \lambda_1^n & S^1(\lambda_1) & \cdots & S^K(\lambda_1) \\ 1 & \lambda_2 & \cdots & \lambda_2^n & S^1(\lambda_2) & \cdots & S^K(\lambda_2) \\ \vdots & \vdots & \vdots & \vdots & \vdots & \vdots & \vdots \\ 1 & \lambda_L & \cdots & \lambda_L^n & S^1(\lambda_L) & \cdots & S^K(\lambda_L) \end{pmatrix} \in \mathbb{R}^{L \times (1+n+K)}, \quad (4)$$

220 Equation 3 can be rewritten as a simple linear fit for each pixel  $(i, j)$ :

$$A \cdot \mathbf{x}(i, j) = \tau(i, j) \quad \forall i, j, \quad (5)$$

whose unknown  $\mathbf{x}(i, j)$  are the concatenation of the polynomial coefficients  $\mathbf{p}(i, j)$  and the dSCDs  $\mathbf{c}(i, j)$  at pixel  $(i, j)$ .

For the NO<sub>2</sub> camera, the value of the measured response (optical thickness  $\tau(i, j)$ ), and of these unknown variables  $\mathbf{x}(i, j)$   
 will vary from pixel to pixel, while the design matrix  $A$  is common to all pixels. As noted earlier, the per-pixel FoV is around  
 225 0.045°. In order to make it comparable to the reference instruments ( $\sim 0.3 \times 1^\circ$  for MAX-DOAS and  $\sim 1.5 \times 1.5^\circ$  for Pandora),  
 a box smoothing is applied to the zenith and the scene using a uniform  $7 \times 23$  or  $33 \times 33$  pixels kernel on each Level-1 intensity  
 map, before computing the optical thickness.

**Table 3.** Parameters and cross-sections used in the DOAS retrieval for each smoothed pixel of the NO<sub>2</sub> camera measurements and for both reference instruments.

Parameter	NO <sub>2</sub> camera	MAX-DOAS	Pandora
Wavelength range	427–454 nm	434–455 nm	435–490 nm
Solar reference	Chance and Kurucz (2010)		
Reference spectra	Fixed reference, zenith on Mar–21 16:03 UTC	Smallest elevation angle	
Intensity offset	None	Linear, degree $\leq 1$	Linear, degree $\leq 1$
Low-order polynomial	Degree $\leq 4$	Degree $\leq 5$	Degree $\leq 4$
<b>Cross-sections:</b>			
– NO <sub>2</sub> (294 K)	Vandaele et al. (1998)		
– Water vapour	HITRAN2012 — Rothman et al. (2013)		
– O <sub>3</sub> (223 K)	Serdyuchenko et al. (2014)		
– O <sub>4</sub> (293 K) (O <sub>2</sub> dimer)	Finkenzeller and Volkamer (2022)	Thalman and Volkamer (2013)	
– Ring effect pseudo-absorber	Wagner et al. (2009)		

The DOAS fitting settings are very close to the recommendations for the NO<sub>2</sub>VIS-SMALL analyses during the CINDI-3 intercomparison campaign (<https://frm4doas.aeronomie.be/index.php/cindi-3>). A notable difference is the wavelength range (427–454 nm versus 411–445nm), which we kept a bit shorter to limit the acquisition time, and which we extended slightly towards longer wavelengths to include additional NO<sub>2</sub> absorption features (visible in Fig. 6). The settings are summarized in Table 3 and an example of retrieval output is shown in Fig. 6.

### 3.4 Characterization of Uncertainties

Considering the NO<sub>2</sub> dSCD as the measurand, we characterize the uncertainty on its estimated values by uncertainty propagation through the measurement model described in the previous sections, starting at its input quantities. In a first attempt, only the random uncertainty in the intensity measurements is considered.

The main random uncertainties affecting the signal (Level-1) measurements come from the CMOS sensor. Following the PTC analysis mentioned earlier, three independent noise components are considered: the read noise, the Poisson shot noise, and the fixed pattern noise. The uncertainty associated with a CMOS output of  $s$  electrons is then

$$u_{\text{CMOS}}(s) = \sqrt{\sigma_{\text{RN}}^2 + s + p_{\text{FPN}}^2 s^2},$$

where  $\sigma_{\text{RN}}^2 = 0.6 \text{ e}^-$  is the variance of the read noise,  $s$  is the variance of the Poisson shot noise, and  $p_{\text{FPN}} = 0.2\%$  is the proportion of FPN. This is valid for the target images as well as the stray light images. At the typical values of input signal (i.e. 5,000 to 60,000  $\text{e}^-$ ), the read noise is negligible compared to shot noise, so we ignore it for the sake of simplicity. As for the FPN, its maximal contribution is obtained when the input signal is highest. For an input of 60,000  $\text{e}^-$ , the uncertainty including 0.2% FPN amounts to 273  $\text{e}^-$  versus 245  $\text{e}^-$  without FPN, which proves that the FPN impact is limited or even negligible depending on the signal level. Moreover, the subtraction of stray light and the division by the PRNU map in Equation 1 have the side

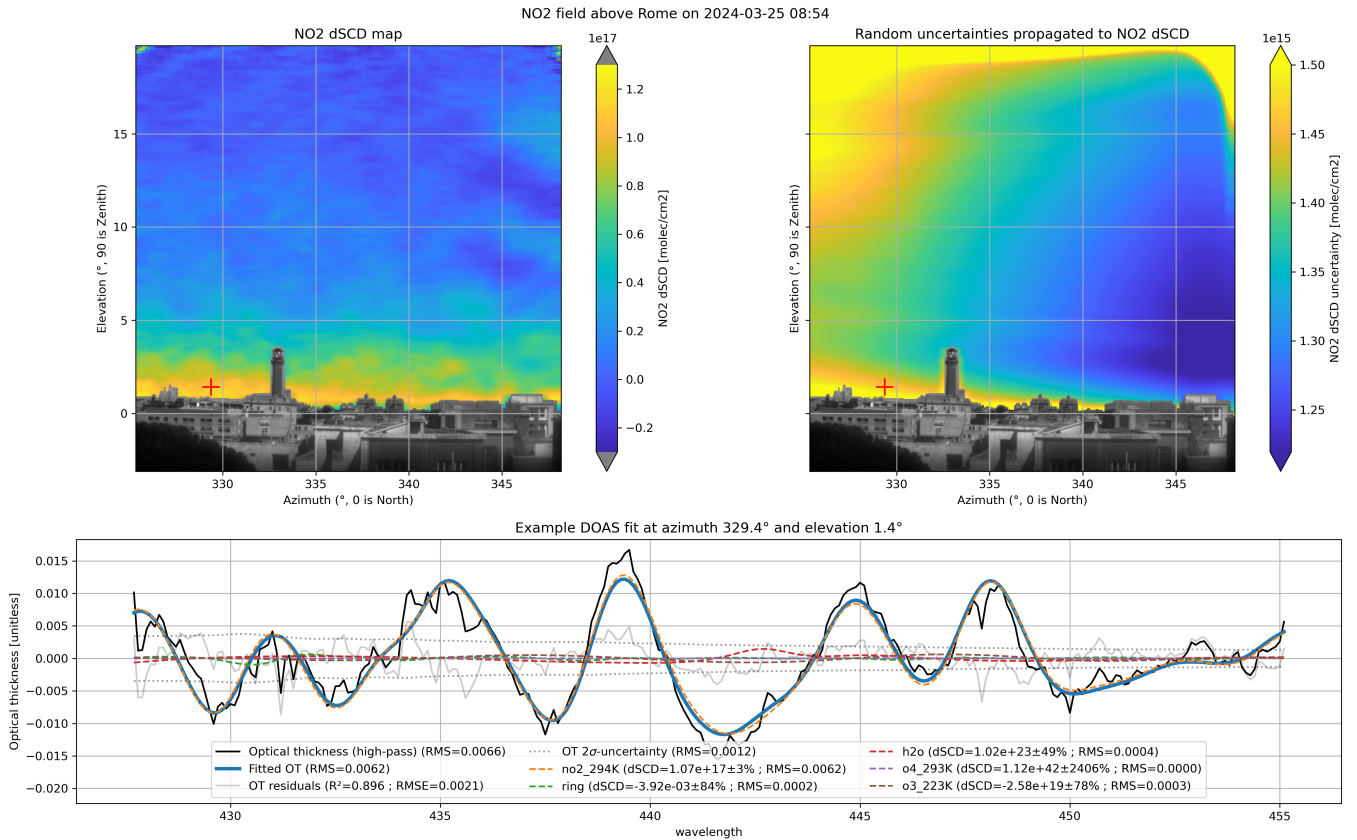


**Figure 6.** Example of output from NO<sub>2</sub> camera retrieval, acquired in Rome on March 25, from 8:55 to 9:01 UTC. The top left panel shows the map of NO<sub>2</sub> dSCDs retrieved for each pixel, while the top right panel shows its estimated uncertainties. In order to give finer spatial context, the pixels under the horizon for both images show the landscape (from the Level-1 data at 455 nm). The bottom panel shows the details of the DOAS fit for one example pixel, marked with a red cross in the top images.

effect of removing the additive and the multiplicative components of FPN, respectively. Potentially remaining FPN would be much smaller and come from non-linear effects which are hard to characterize. For this reason, FPN is also ignored, and the standard uncertainty of the Level-1 signal,  $u_{L1}$ , is

$$u_{L1}(\lambda, i, j) \simeq \frac{1}{\text{PRNU}(i, j)} \sqrt{G S(\tilde{\lambda}, i, j) + G S_0(i, j)}.$$

In this equation,  $G$  is again the detector's gain,  $S$  the L0 signal intensity, and  $S_0$  the L0 stray light signal as defined in Eq. 1. While we do expect close values of  $I_{L1}(\lambda, i, j)$  for neighboring wavelengths and pixels, we assume that their measurement errors are statistically independent. Therefore, we do not consider the covariance structure among the measurement errors at different pixels and wavelengths in the signal. We also hypothesize that the target and zenith cubes are independent. We are aware of the limiting aspect of these assumptions: we will address them in future developments, and an empirical approach is proposed for the campaign results presented in this work. Propagating these random uncertainties in the definition of optical

thickness (including the preliminary box-smoothing intensities with size  $k \times k$ ) gives the uncertainty on the optical thickness,

$u_\tau$ :

$$245 \quad u_\tau(\lambda, i, j) = \sqrt{\frac{u_{L1}^2(\lambda, i, j)}{k^2 I_{L1}^2(\lambda, i, j)} + \frac{u_{z,L1}^2(\lambda, i, j)}{k^2 I_{z,L1}^2(\lambda, i, j)}} \approx \frac{1}{k} \sqrt{\frac{1}{I_{L1}(\lambda, i, j)} + \frac{1}{I_{z,L1}(\lambda, i, j)}}, \quad (6)$$

where  $I_{z,L1}$  and  $u_{z,L1}$  are respectively the intensity and uncertainty of the zenith measurements. The last approximation is valid when the stray light intensity is small compared to the target image.

Assuming that the DOAS design matrix  $A$  is perfectly known, the uncertainty on  $\tau(x, y)$  propagates to the dSCDs and polynomial coefficients as the following covariance matrix:

$$250 \quad \Sigma_{\mathbf{x}(i,j)} = (A^\top \text{diag}(1/u_\tau^2(i,j)) A)^{-1}. \quad (7)$$

Returning the full covariance structure for each pixel is not practical for the data users, therefore only the square root of the diagonal terms is reported:

$$\mathbf{u}_x(i, j) = \sqrt{\text{diag}(\Sigma_{\mathbf{x}(i,j)})}. \quad (8)$$

This produces a one-dimensional uncertainty estimate for the  $\text{NO}_2$  dSCD at each pixel, which we can display in a map similarly  
 255 to the dSCDs themselves, as shown in Fig. 6. The residuals of the DOAS spectral fit show some non-random structure and are regularly larger than the estimated uncertainty on optical thickness. This shows that our estimation underestimates the true total uncertainty, which was expected because we ignored the systematic contributions.

An in-depth assessment of systematic uncertainties is outside of the scope of this paper. However some preliminary analyses showed that a small error of 0.01 nm in the wavelength alignment might propagate to an error of  $5e15$  molec/cm<sup>2</sup> on the  $\text{NO}_2$   
 260 dSCD. Therefore we expect the wavelength alignment to be a major contributor to the  $\text{NO}_2$  dSCD uncertainties. Improper stray light removal might be another important source of systematic uncertainty, since the optical thickness would be multiplied by a factor close to  $(1 - I_{\text{stray}}(\lambda)/I_0(\lambda))$  (Platt and Stutz, 2008, p.327), hence also influencing all dSCDs. If the remaining stray light intensity in the Level-1 image is about 2 % (positive or negative), this could impact the  $\text{NO}_2$  dSCD by up to  $\pm 4e15$  molec/cm<sup>2</sup>. Finally, Vandaele et al. (1998) report an uncertainty  $\leq 3$  % on the  $\text{NO}_2$  cross-section, which might also contribute  
 265 to the dSCD uncertainty. A full error budget for the instrument will be worth a separate publication when it is completed.

## 4 Campaign in Rome

### 4.1 Objectives

In Rome, the Atmospheric Physics Laboratory (APL) of Sapienza University hosts the BAQUNIN super site (Boundary-layer Air Quality-analysis Using Network of INstruments), where several ground-based instruments are available that monitor the

270 boundary layer air quality (Iannarelli et al., 2022). This urban observatory is equipped to host ground-based instruments such as the NO<sub>2</sub> camera for inter-comparison/inter-calibration campaigns. It was selected as location for a first urban test campaign in a challenging environment showing strong spatial and temporal variations.

The goal of the measurement campaign in Rome is to validate the correctness of the NO<sub>2</sub> camera retrievals with two state-of-the-art remote sensing instruments: a Pandora and a MAX-DOAS, described hereafter. Both of these reference instruments measure dSCDs. By performing a light path assessment (e.g. using O<sub>4</sub> absorption), and the inversion of NO<sub>2</sub> concentration vertical profiles, their results can typically be converted to NO<sub>2</sub> concentrations. As this paper focuses on the measurement and operational principle of the NO<sub>2</sub> camera rather than on the processing of the results, only NO<sub>2</sub> dSCDs are compared between the different reference instruments and the NO<sub>2</sub> camera. The light path assessment, the inversion of the vertical profile, and the resulting NO<sub>2</sub> concentration have a high priority on the NO<sub>2</sub> camera roadmap through a pending integration into the FRM4DOAS framework (Van Roozendaal et al., 2024) but are outside of the scope for this paper.

## 4.2 Reference NO<sub>2</sub> remote sensing instruments

### 4.2.1 MAX-DOAS

The MAX-DOAS instrument used for the campaign is a SkySpec-2D system by Airyx. This system has been acquired by CNR-ISAC in 2021 and operated from the CIRAS (CNR Isac Rome Atmospheric obServatory), in the CNR research area of Tor Vergata since September 2021. The instrument is composed of a telescope (installed outdoors), a spectrometer unit, and a measurement PC. The spectrometer is connected to the telescope via an optical fiber. The spectrometer unit contains two spectrometers that simultaneously acquire the spectra in the UV and VIS spectral ranges at a high spectral resolution. The prism telescope covers elevation angles from -10° to 190°. The 2D model allows the user to measure at different azimuth angles.

290 The instrument was transferred from CIRAS to BAQUNIN and installed on the roof of APL, on another platform about 5 meters away and lower than the Pandora and NO<sub>2</sub> camera. The measurements were analyzed using QDOAS software and the same parameters as in (Pettinari et al., 2022). These parameters are summarized in Table 3 for convenience.

### 4.2.2 Pandora

Pandora-2S instruments are fiber-fed hyperspectral spectrometers mounted on a microprocessor-controlled azimuth/elevation tracker and manufactured by SciGlob LLC (Elkridge, MD, USA). They are regrouped in the Pandonia Global Network (PGN), which is co-funded by NASA and ESA and operated by LuftBlick OG (Innsbruck, Austria). The instrument present at the BAQUNIN-APL supersite has identifier PAN#117.

For each day of PAN#117 measurements, a set of level-2 fit files is produced by the PGN centralized processing, each corresponding to a specific measurement mode and target species. Because the campaign focused on NO<sub>2</sub>, the “nvh3” data product was analyzed. A detailed description of the fit, its parameters, and its outputs is provided in Cede et al. (2025) and

summarized in Table 3 for convenience. The uncertainty estimates of the retrieved NO<sub>2</sub> dSCDs were obtained by combining in quadrature their independent, structured and common uncertainties.

### 4.2.3 Differences in retrievals parameters

The retrieval parameters of the different instruments are listed in Table 3. Even though differences in retrieval settings can cause inter-instrumental differences, we have opted to keep the settings of the reference instruments the same as in earlier published results.

The summary in Table 3 underlines some inter-instrumental differences in DOAS parameters. This results from a will to reuse prescribed settings from published results from each instrument separately. This is a potential cause for inter-instrumental differences in retrieved dSCDs.

In particular, the agreement on a reference spectrum is crucial to compare dSCDs from several DOAS instruments. The NO<sub>2</sub> camera and the MAX-DOAS used a fixed zenith reference acquired on the 21st of March at 16:00 UTC for all their dSCDs. The Pandora, on the other hand, relies on centralized processing within PGN to obtain an NO<sub>2</sub> dSCD. It is thus based on a sequential reference, defined as the spectrum taken at the lowest viewing elevation angle during each azimuthal scan (Cede et al., 2025, Product nvh3). Most of its dSCDs are then expected to be negative, requiring a post-processing step for comparability.

The difference in reference between the instruments could be compensated by computing a correction term for each Pandora azimuthal scan and adding it to all dSCDs in the scan. To compute this term, we compared the Pandora zenith dSCD during each scan with the corresponding (time-interpolated) retrieval of the MAX-DOAS. Their difference was added to all dSCDs at all viewing elevation angles in the same azimuthal scan from Pandora. When the scan contains several zenith observations, the averaged difference was used. This correction was also accounted for in the uncertainty estimates.

The difference in O<sub>4</sub> cross-section is not expected to have a strong influence on the comparison results since we focus on the NO<sub>2</sub> dSCD without performing the inversion to concentration profiles.

Finally, another significant difference between the instruments is the longer wavelength range used by the Pandora. We do believe it has an impact on the comparison results: this longer range is expected to include photons with a longer optical path, hence increasing the Pandora's dSCDs. However, we preferred to adhere to the well-validated operational settings of the international PGN network to retain its value as a reference instrument.

## 4.3 Acquisition plan

Four primary azimuth angles were selected for the actual measurement campaign: 27°, 124°, 130°, and 340°. Sample images showing the scenes in the different azimuth directions are shown in Fig. 7. Each different azimuth represents a different type of environment. In the direction of 27° and 340°, the area is mostly residential, whereas 124° and 130° are mixed residential and industrial zones. For the latter azimuth directions, the optical path is limited by the mountains for parts of the image. The tower that is clearly visible in the image taken in the 340° direction was used to calibrate the pointing of each instrument.

After a calibration and test phase in the beginning of the campaign, the Pandora and MAX-DOAS started sampling the NO<sub>2</sub> field inside the field of view of the NO<sub>2</sub> camera. This allows the user to reconstruct a two-dimensional NO<sub>2</sub> dSCD map for each instrument. Fig. 7b highlights these sample points for both the MAX-DOAS and Pandora.

In both azimuth and elevation, the Pandora samples every 1°. A denser spatial sampling is not necessary as the field of view of the Pandora is roughly a circle of 1.5° diameter. The MAX-DOAS has a field of view of around 0.3° vertically by 1° horizontally. Therefore, a measurement was taken every 0.5° in elevation angle and every 1° horizontally.

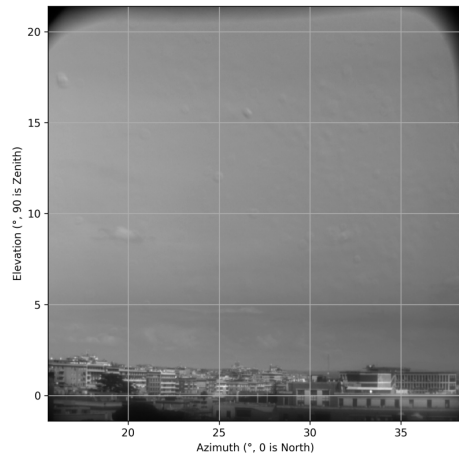
## 5 Campaign results

### 340 5.1 Comparison methodology

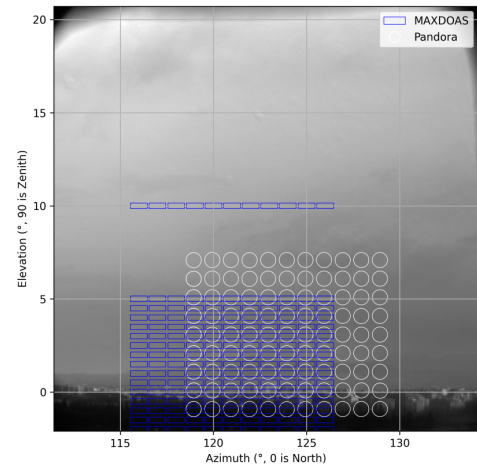
For every Pandora and MAX-DOAS measurement, the closest NO<sub>2</sub> camera pixel in space is determined. For this pixel, the dSCD value is compared to the results of the Pandora and MAX-DOAS. Both in azimuth and elevation, a tolerance of 0.1° was allowed. When the pointing correction is applied correctly, the elevation angle and the time difference remain the two parameters that influence the quality of the correlation the most, as we will now discuss.

345 Fig. 8a shows all the dSCDs measured by both the MAX-DOAS and their corresponding dSCD retrieved by the NO<sub>2</sub> camera. For this comparison, a maximum time difference of 30 minutes is allowed between the MAX-DOAS and the NO<sub>2</sub> camera measurement. The different measurement points are colored according to the elevation angle at which they are measured. Ideally, all measured points would lie on the diagonal: both dSCDs would be equal in this case. The dots colored in red indicate elevation angles well below the horizon (-1°). The dots colored in yellow are measurement points between -1° and 1°. The green dots show the measurements for elevation angles higher than 1°. Values outside the limits of the axes are clipped to the axis limit. The different colors demonstrate that, for low elevation angles, the correlation between the MAX-DOAS and the NO<sub>2</sub> camera is significantly worse than for higher elevation angles. As the figure for the Pandora is very similar, but with fewer data points available, this image is not shown here. This is due to the presence of buildings (visible in Fig. 7), inducing much shorter light path for some instruments. Because the instruments were located a few meters away from each other (including a difference in elevation for the MAX-DOAS), the parallax error leads to differences in the observed scenes. For the remainder of the paper, we will remove from the comparison all points that are at or below 1°.

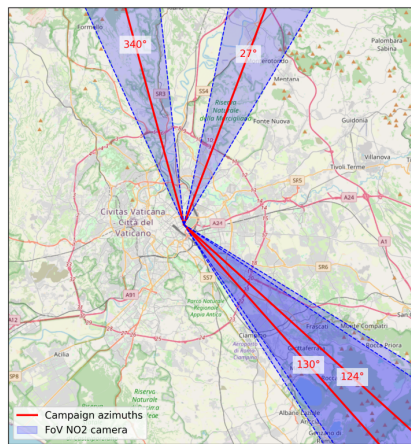
For Fig. 8a, a maximum of 30 minutes was allowed between the MAX-DOAS and the NO<sub>2</sub> camera measurement. This time difference has a significant impact on the comparison between the instruments. Fig. 8b illustrates this influence. Here, only elevation angles above 1° are shown. The less stringent the time requirements become, the more spread out the values are. Values outside the limits of the axes are again clipped to the axis limit. This illustrates that the NO<sub>2</sub> field presents dynamic patterns at the scale of minutes. Therefore, we restrict the time tolerance to ±5 minutes for the comparisons in this paper.



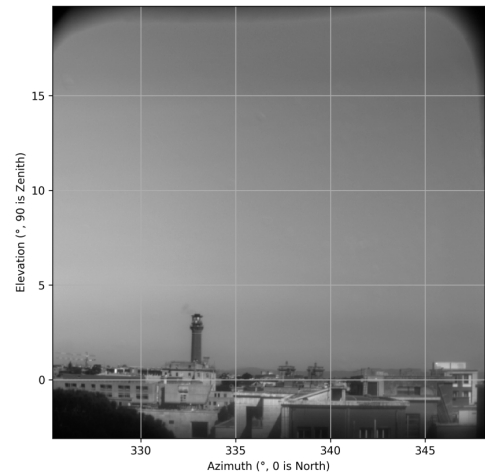
(a)



(b)



(c)



(d)

**Figure 7.** Representative spectral images (at 460 nm) of the main azimuth directions observed during the campaign, with (a) 27°, (b) 124°, and (d) 340° respectively. Each one covers a different type of environment. In addition, panel (b) shows the spatial sampling of the Pandora and MAX-DOAS within the field of view of the NO<sub>2</sub> camera is illustrated. For the sake of readability, this is not shown on the other scenes. Panel (c) shows the four main azimuths used during the measurement campaign. The shaded area in blue shows the field of view of the camera. For 124° and 130°, the camera takes pictures in the direction of 126° and 128° respectively. This allows us to have more comparison points with the other instruments. Map data in Panel (c) © OpenStreetMap contributors, licensed under the Open Database License (ODbL).

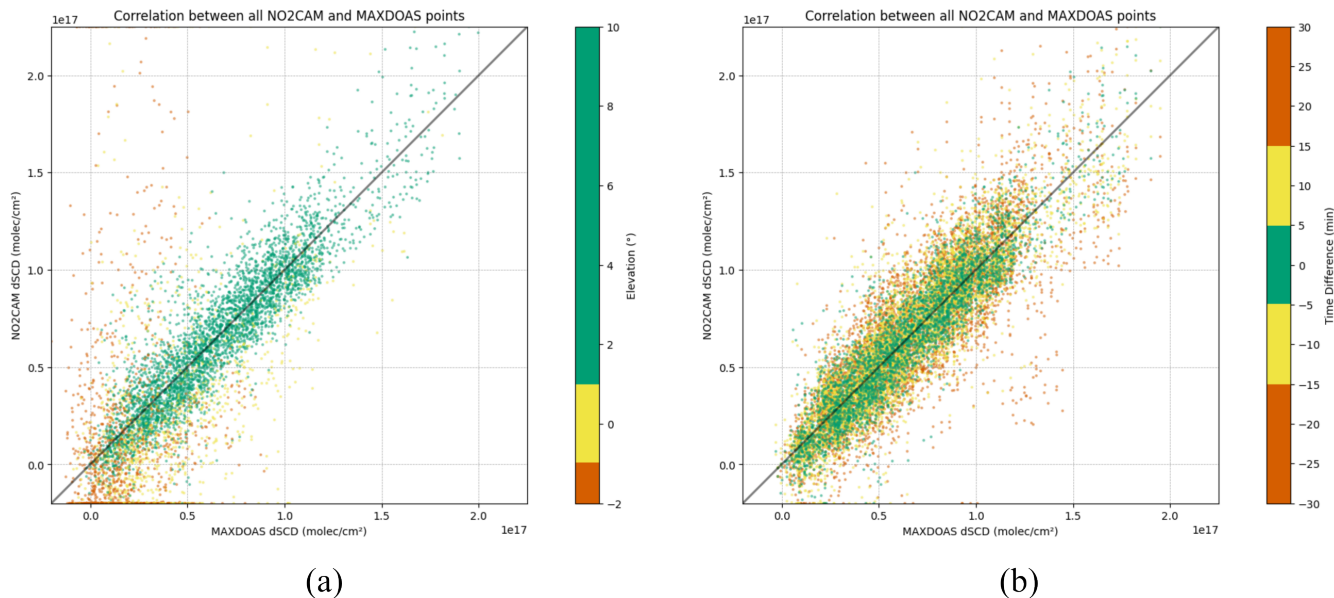


**Figure 8.** Comparing dSCDs between the NO<sub>2</sub> camera and the MAX-DOAS shows the strong impact of measurements under the horizon and of large differences in measurement timestamps. Panel (a) shows that the low elevation points differ more significantly from the diagonal than the points above 1° (green versus red). Panel (b) focuses on elevation above 1° and shows that the allowed time difference for the comparison strongly influences the results: smaller time differences have better correspondence (green versus red). In both panes, values outside the viewing window are clipped to the viewing window border.

## 5.2 Comparison results

Before comparing the NO<sub>2</sub> camera with each reference instrument, we first present a baseline comparison between the MAX-DOAS and the Pandora results. The purpose of this analysis is to set a baseline for the quality of the main comparisons, involving the NO<sub>2</sub> camera. Even though both reference instruments have already been extensively validated, we do expect some differences in the results because of the imperfect time synchronization and the different DOAS settings, as explained in Section 4.2.3. A simple difference and a linear regression were used to characterize the relation between the Pandora and MAX-DOAS dSCDs, after applying the data filters discussed in the previous section. These statistics were calculated globally on all azimuth directions and outliers outside the interval  $[-2e16, 2e17]$  molec/cm<sup>2</sup> were excluded for the regression.

Due to small differences in the scanning schedule of the Pandora and MAX-DOAS, this direct comparison includes only 69 measurement points, much less than the comparisons involving the NO<sub>2</sub> camera. The results, presented in Fig. 9, show a root-mean-square error (RMSE) of  $7e15$  molec/cm<sup>2</sup> and a mean bias of  $2e15$  molec/cm<sup>2</sup>. The line of best fit has a slope of  $0.99 \pm 0.04$  and an  $R^2$  value of 0.97. In this direct comparison, we would actually expect a regression slope above 1, due to the longer wavelength range used in the Pandora. However, the very limited number of points might have prevented us from observing it, as shown by the confidence interval.

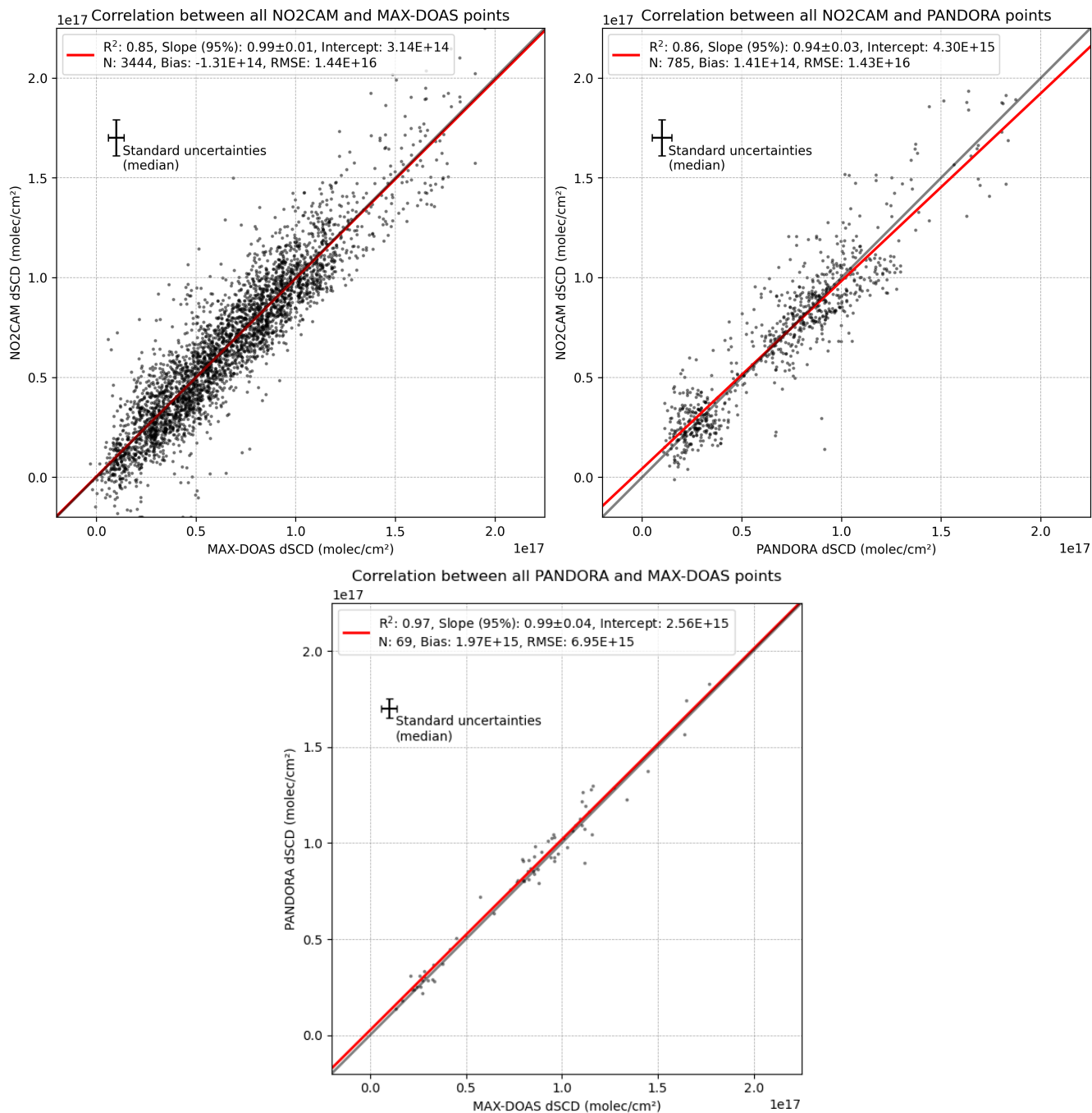


**Figure 9.** Scatterplots comparing the NO2 camera with the MAX-DOAS (upper left panel) and Pandora (upper right panel), including a linear regression for each. Measurement points were filtered to elevations above 1° (strictly) and time difference under 5 minutes. The lower panel shows a direct comparison of the MAX-DOAS and Pandora, using the same filters, which serves as a baseline.

The main analysis compared the NO<sub>2</sub> camera to each reference instrument, computing a simple difference and a linear regression with the same methodology as the baseline analysis. The summary statistics are detailed in Table 4. In particular, the root-mean-square error (RMSE) obtained is 1.4e16 molec/cm<sup>2</sup> compared to both references, and the mean bias is very small, at 1.3e14 molec/cm<sup>2</sup> (MAX-DOAS) and 1.4e14 molec/cm<sup>2</sup> (Pandora). The regressions and the corresponding scatter plots are shown in Fig. 9. The regression slope obtained is 0.99 for the comparison with MAX-DOAS. For Pandora, the slope is 0.94, which is significantly smaller than unity. A possible explanation is the Pandora’s longer wavelength range.

**Table 4.** Summary statistics on the comparison of the camera’s NO<sub>2</sub> dSCDs compared to each reference instrument, on all common retrievals from the campaign.

	MAX-DOAS	Pandora
Number of observation pairs	3445	785
NO <sub>2</sub> camera bias (mean difference) [molec/cm <sup>2</sup> ]	1.3e14	1.4e14
Root-mean-square error [molec/cm <sup>2</sup> ]	1.4e16	1.4e16
<b>Linear regression</b>		
– Slope (95% CI)	0.99±0.01	0.94±0.03
– Intercept [molec/cm <sup>2</sup> ]	3.1e15	4.3e15
– Coefficient of determination (R <sup>2</sup> )	0.85	0.86

### 5.3 Imaging results

Example images of the dSCDs measured in the different azimuthal directions are shown in Fig. 10. In these figures, fine structures in the NO<sub>2</sub> field can be distinguished. As expected, lines of sight grazing the horizon are capturing much higher NO<sub>2</sub> dSCDs. The imaging quality of the NO<sub>2</sub> camera also reveals horizontal and vertical gradients. An interesting case is, for instance, the enhancement on the left side of Fig. 10b, which should be further investigated. In addition, some figures show artifacts in the upper part of the image. These artifacts are created by the moving clouds or aerosols, whereas the lower region of the image is left unaffected.

In addition to the quantitative comparison shown in Table 4, a qualitative comparison can also be made with the reference instruments. Fig. 11 shows a NO<sub>2</sub> dSCD map taken in the direction of 124°, with overlays showing the corresponding MAX-DOAS and Pandora dSCDs. Similar patterns are found with all three measurement instruments.

### 5.4 Uncertainties

Previous sections have already described the methodology followed by each instrument for uncertainty estimation. Table 5 presents summary statistics on the resulting estimated errors. As already mentioned, systematic or structured uncertainties are not (yet) considered for the NO<sub>2</sub> camera retrievals, so we expect serious underestimation of uncertainty. As a pragmatic alternative, we also report the standard deviation of NO<sub>2</sub> dSCDs among all pixels from the same elevation and same cube,

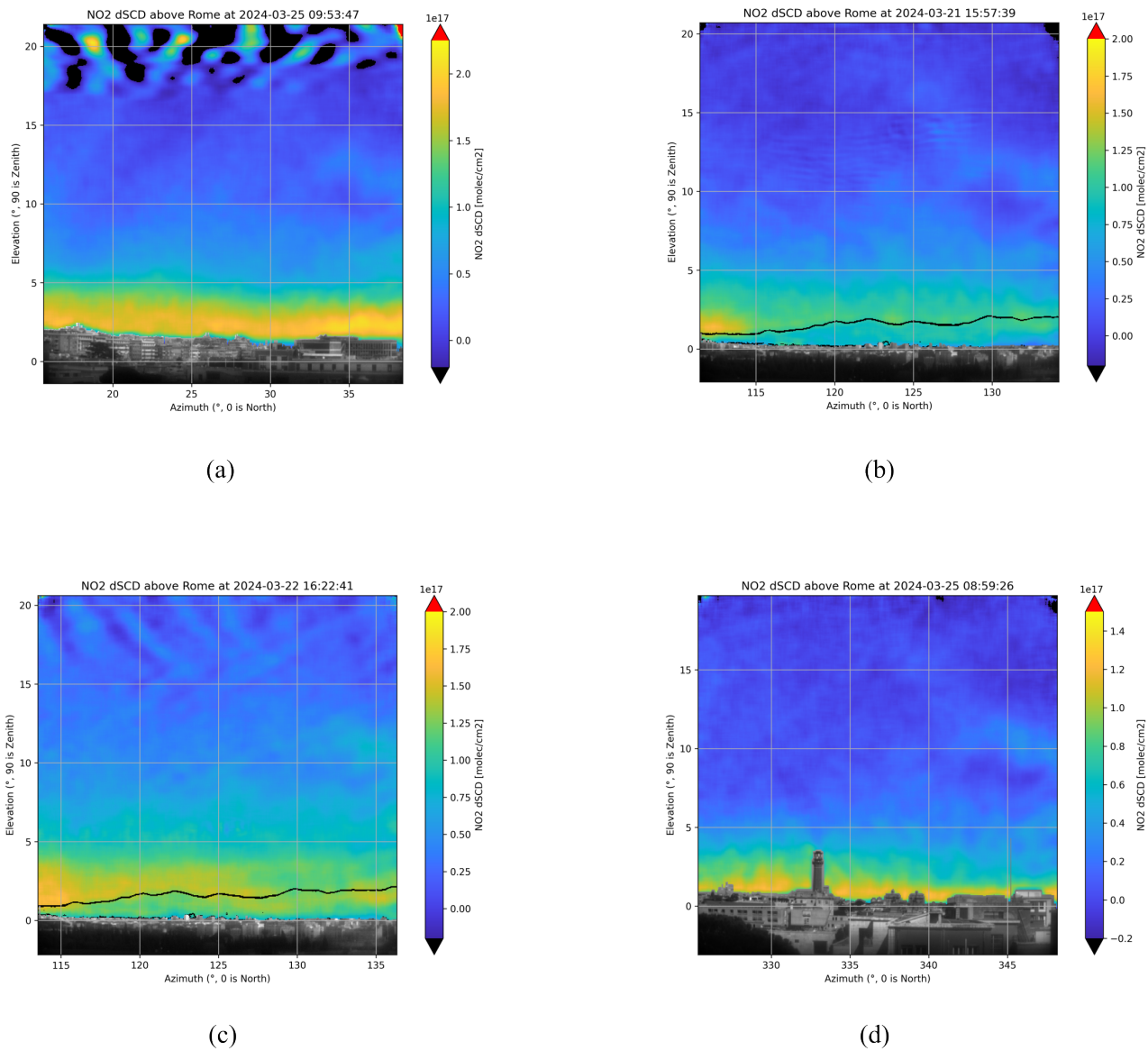


**Figure 10.** NO<sub>2</sub> dSCD maps for the four main azimuth directions in the measurement campaign. Note the different scales for the different directions. All times shown are UTC. On panes (a) and (c), the effects of moving clouds or aerosols are visible at the top of the image.

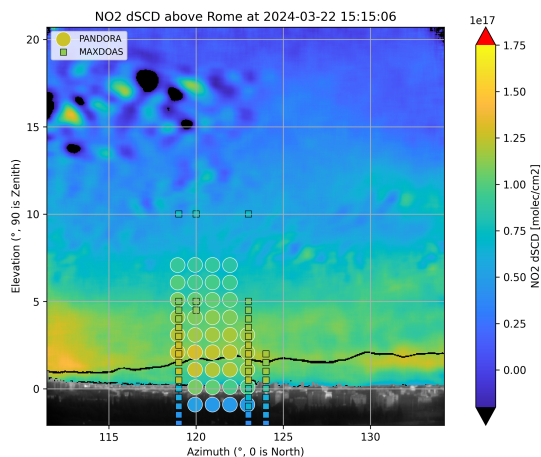


**Figure 11.** Qualitatively, the  $\text{NO}_2$  dSCDs of both the Pandora and MAX-DOAS agree well with the dSCD obtained with the  $\text{NO}_2$  camera. The size of the dots is not representative for the field of view of the instruments.

which we consider to be an empirical estimate of retrieval errors. This probably over-estimates the uncertainty, especially at low elevations, since it also includes the true azimuthal variation of the  $\text{NO}_2$  field. On the other hand, the empirical indicator might under-estimate the uncertainty in case of a systematic bias. However, the comparison with the other instruments in Fig. 9  
400 did not reveal any such bias, so we believe this empirical approach is valuable.

**Table 5.** Statistics on  $\text{NO}_2$  dSCD uncertainty estimates for the whole campaign for each instrument, computed globally across all included elevation angles.

Instrument	Uncertainty ( $\times 10^{15}$ molec/cm <sup>2</sup> )
	<i>Median [95% coverage range]</i>
$\text{NO}_2$ camera (from shot noise)	1.3 [0.5–1.7]
$\text{NO}_2$ camera (empirical)	9 [4–26]
MAX-DOAS	4 [3–6]
Pandora	5 [3–10]

## 6 Conclusions

We have presented the results of an intercomparison campaign between the  $\text{NO}_2$  camera, an AOTF-based spectral imager optimized for the measurement of  $\text{NO}_2$  slant column densities (SCD) from the scattered solar light in the 425–455 nm domain, and two reference diffraction grating-based spectrometers: a MAX-DOAS, and a Pandora. The three instruments were deployed  
405 in March 2024 at the BAQUNIN supersite on top of the physics department building of the Sapienza university, located in the center of Rome, Italy. They were operated in such a way that the field of view of the  $\text{NO}_2$  camera was sampled by the two

other instruments at different azimuths, and under strict coincidence criteria. The focus was on the NO<sub>2</sub> distribution close to the horizon, where local sources and winds are shaping the NO<sub>2</sub> field. Given the unconventional concept of the NO<sub>2</sub> camera where wavelengths are acquired sequentially rather than simultaneously, the first and main purpose of the campaign was to validate its measured NO<sub>2</sub> SCDs with the coincident observations of the reference instruments. The secondary objectives were: (1) to demonstrate that the NO<sub>2</sub> camera hyperspectral cubes can be processed by the DOAS method, the leading technique for the processing of UV–visible light spectra; and (2) to illustrate the capabilities of the NO<sub>2</sub> camera in revealing the spatial and temporal gradients of an urban NO<sub>2</sub> field.

The primary objective was achieved through the analysis of hundreds of coincident observations, which revealed that large NO<sub>2</sub> dSCDs ( $> 2 \times 10^{16}$  molec/cm<sup>2</sup>) are usually well retrieved by the NO<sub>2</sub> camera. Those are typically found at low elevation angles, where the light crosses air masses of high NO<sub>2</sub> concentrations over long distances. Comparison of coincident observations with the MAX-DOAS and the Pandora for elevations up to 10° shows good agreement ( $R^2 = 0.86$  for both), demonstrating that the NO<sub>2</sub> camera can provide meaningful quantitative information.

All of the camera acquisitions were performed in a "DOAS mode", a driving scheme in which the AOTF bandpass filter is swept by small steps (0.15 nm) across a wavelength range in order to obtain *continuous spectra*. Contrary to diffraction grating-based instruments, regularly sampling a chunk of optical spectrum with fine steps requires an excellent control of the AOTF. In general, no problem was found in applying the DOAS method, confirming the good tuning performance of the instrument. The main problems encountered were related to the stability of the shape of the AOTF response function, and to changes of illumination conditions during the acquisitions, affecting the obtained NO<sub>2</sub> dSCDs.

While capturing spatial gradients is easy for a native imaging system such as the NO<sub>2</sub> camera, observations of extended scenes are not routinely performed by conventional operational air quality remote sensing instruments such as the MAX-DOAS and the Pandora spectrometers. It requires the sequential pointing of the collecting optics in many pairs of azimuth and elevation angles. On the other hand, the light spectrum is captured at once. The *images*, eventually produced based on the results of the MAX-DOAS and Pandora measurements, lack details usually helpful for understanding the context of the observations or seeing fine-scale features. The 20° × 20° field of view of the NO<sub>2</sub> camera could only be sampled by the other two instruments at the price of long acquisition sequences. The variation of the temporal coincidence criteria, between ±5 and ±30 minutes, highlights the temporal variability of the urban NO<sub>2</sub> field, be it driven by changes in the emissions, light path, or in illumination conditions. In some scenes, local enhancements are clearly captured by the imager, revealing spatial gradients which would be hard to see with the other ground-based instruments.

These encouraging results are calling for further usage of the NO<sub>2</sub> camera. First, the few local and transient enhancements which have already been detected are just a glimpse of the many more "pollution events" that can happen in an urban environment such as Rome. Long-term installation of the instrument as part of a supersite like BAQUNIN would allow for studying these events in order to understand their origin, their amplitude, their correlation with changes in the light path, and the fate of the plume. Second, the tuning range of the instrument is not limited to 425–450 nm, such that the acquisition of spectral images in a region of strong O<sub>4</sub> absorption (470–480 nm) would allow for informing on the visual range of the pixel line of sight. This information will be required in order to retrieve tropospheric NO<sub>2</sub> columns from the NO<sub>2</sub> dSCD maps measured

by the camera. Finally, the instrument itself can be improved further, mainly by increasing the frame-rate of the detector, better characterizing the spectral response function, and reducing the internal stray light.

445 *Data availability.* All data points from the campaign in Rome which were used to compare the NO<sub>2</sub> camera to each reference instrument is published on BIRA-IASB's data repository in August 2025 and accessible at URL <https://doi.org/10.18758/epcuyj7z>. Given their important volume, the full-resolution data from the NO<sub>2</sub> camera during the campaign will *not* be included there, but are available by request to the corresponding authors.

450 *Author contributions.* PG, CB and ED developed the NO<sub>2</sub> camera, operated it during the campaign, processed its data, performed the instruments comparison and wrote the manuscript. DP wrote driver software for NO<sub>2</sub> camera. NB, SC, ADB, PP, EC reviewed the manuscript. SC, AMI and PP operated the reference instruments and processed their data. ADB and NF provided technical and logistic support for the campaign. LDL, FC are the principal investigators of the MAX-DOAS instrument.

*Competing interests.* All authors declare having no competing interests.

455 *Acknowledgements.* This work was performed in the frame of the Instrument Data Quality Evaluation and Assessment Service – Quality Assurance for Earth Observation (IDEAS-QA4EO) contract funded by ESA-ESRIN (n. 4000128960/19/I-NS). We are grateful to Angelika Dehn and Philippe Goryl (ESA-ESRIN GMQ) for their invaluable support to this activity.

The SkySpec-2D system was acquired under the project “Sviluppo delle Infrastrutture e Programma Biennale degli Interventi del Consiglio Nazionale delle Ricerche—Potenziamento Infrastrutturale: progetti di ricerca strategici per l'ente. Progetto 55—ASSE CENTRO”.

460 The authors would like thank our colleagues Michel Van Roozendael and his team for the valuable feedback on early results and for the QDOAS software, David Bolsée and Nuno Pereira for their help obtaining the PTC curve of the detector, and the engineering department of BIRA-IASB for their support. Manuel Roca and Axel Kreuter from LuftBlick OG gave very appreciated support in the operation and data processing of the Pandora instrument. The authors would also like to thank Dimitris Karagkiozidis for making his EKO library available to them. Lastly, the authors wish to thank two anonymous reviewers for their detailed and useful comments.

## References

- Cede, A., Tiefengraber, M., Gebetsberger, M., and Spinei Lind, E.: Pandonia Global Network Data Products Readme Document, LuftBlick, 465 [https://www.pandonia-global-network.org/wp-content/uploads/2025/01/PGN\\_DataProducts\\_Readme\\_v1-8-10.pdf](https://www.pandonia-global-network.org/wp-content/uploads/2025/01/PGN_DataProducts_Readme_v1-8-10.pdf), 2025.
- Chance, K. and Kurucz, R.: An improved high-resolution solar reference spectrum for earth's atmosphere measurements in the ultraviolet, visible, and near infrared, *Journal of Quantitative Spectroscopy and Radiative Transfer*, 111, 1289–1295, <https://doi.org/10.1016/j.jqsrt.2010.01.036>, 2010.
- Chang, I. C.: Noncollinear acousto-optic filter with large angular aperture, *Applied Physics Letters*, 25, 370–372, 470 <https://doi.org/10.1063/1.1655512>, 1974.
- Chen, X., Qi, L., Li, S., and Duan, X.: Long-term NO<sub>2</sub> exposure and mortality: A comprehensive meta-analysis, *Environmental Pollution*, 341, 122971, <https://doi.org/10.1016/j.envpol.2023.122971>, 2024.
- De Craemer, S., Vercauteren, J., Fierens, F., Lefebvre, W., and Meysman, F. J. R.: Using Large-Scale NO<sub>2</sub> Data from Citizen Science for Air-Quality Compliance and Policy Support, *Environmental Science & Technology*, 54, 11070–11078, 475 <https://doi.org/10.1021/acs.est.0c02436>, 2020.
- Dekemper, E., Loodts, N., Van Opstal, B., Maes, J., Vanhellemont, F., Matshvili, N., Franssens, G., Pieroux, D., Bingen, C., Robert, C., De Vos, L., Aballea, L., and Fussen, D.: Tunable acousto-optic spectral imager for atmospheric composition measurements in the visible spectral domain, *Appl. Opt.*, 51, 6259–6267, <https://doi.org/10.1364/AO.51.006259>, 2012.
- Dekemper, E., Vanhamel, J., Van Opstal, B., and Fussen, D.: The AOTF-based NO<sub>2</sub> camera, *Atmospheric Measurement Techniques*, 9, 6025–6034, <https://doi.org/10.5194/amt-9-6025-2016>, 2016. 480
- Finkenzeller, H. and Volkamer, R.: O<sub>2</sub>–O<sub>2</sub> CIA in the gas phase: Cross-section of weak bands, and continuum absorption between 297–500 nm, *Journal of Quantitative Spectroscopy and Radiative Transfer*, 279, 108063, <https://doi.org/10.1016/j.jqsrt.2021.108063>, 2022.
- Fussen, D., Baker, N., Deboscher, J., Dekemper, E., Demoulin, P., Errera, Q., Franssens, G., Matshvili, N., Pereira, N., Pieroux, D., and Vanhellemont, F.: The ALTIUS atmospheric limb sounder, *J. Quant. Spectrosc. Radiat. Transf.*, <https://doi.org/10.1016/J.JQSRT.2019.06.021>, publisher: Pergamon, 2019. 485
- Harris, S. E. and Wallace, R. W.: Acousto-Optic Tunable Filter, *J. Opt. Soc. Am.*, 59, 744, <https://www.osapublishing.org/josa/abstract.cfm?id=53721>, 1969.
- Herman, J., Cede, A., Spinei, E., Mount, G., Tzortziou, M., and Abuhassan, N.: NO<sub>2</sub> column amounts from ground-based Pandora and MFDOAS spectrometers using the direct-sun DOAS technique: Intercomparisons and application to OMI validation, *Journal of Geophysical Research: Atmospheres*, 114, <https://doi.org/10.1029/2009JD011848>, <https://onlinelibrary.wiley.com/doi/pdf/10.1029/2009JD011848>, 2009. 490
- Heue, K.-P., Wagner, T., Broccardo, S. P., Walter, D., Piketh, S. J., Ross, K. E., Beirle, S., and Platt, U.: Direct observation of two dimensional trace gas distributions with an airborne Imaging DOAS instrument, *Atmospheric Chemistry and Physics*, 8, 6707–6717, 495 <https://doi.org/10.5194/acp-8-6707-2008>, 2008.
- Huangfu, P. and Atkinson, R.: Long-term exposure to NO<sub>2</sub> and O<sub>3</sub> and all-cause and respiratory mortality: A systematic review and meta-analysis, *Environment International*, 144, 105998, <https://doi.org/10.1016/j.envint.2020.105998>, 2020.
- Iannarelli, A. M., Di Bernardino, A., Casadio, S., Bassani, C., Cacciani, M., Campanelli, M., Casasanta, G., Cadau, E., Diémoz, H., Mevi, G., Siani, A. M., Cardaci, M., Dehn, A., and Goryl, P.: The Boundary Layer Air Quality-Analysis Using Network of Instruments (BAQUNIN)

- 500 Supersite for Atmospheric Research and Satellite Validation over Rome Area, *Bulletin of the American Meteorological Society*, 103, E599–E618, <https://doi.org/10.1175/bams-d-21-0099.1>, 2022.
- Janesick, J. R.: Photon transfer, no. PM170 in SPIE Press monograph, SPIE, Bellingham, Wash. <1000 20th St. Bellingham WA 98225-6705 USA>, ISBN 9780819478382, restricted to subscribers or individual electronic text purchasers, 2007.
- Kuhn, J., Platt, U., Bobrowski, N., and Wagner, T.: Towards imaging of atmospheric trace gases using Fabry–Pérot interferometer correlation spectroscopy in the UV and visible spectral range, *Atmos. Meas. Tech.*, 12, 735–747, <https://doi.org/10.5194/amt-12-735-2019>, publisher: Copernicus GmbH, 2019.
- 505 Kuhn, L., Kuhn, J., Wagner, T., and Platt, U.: The NO<sub>2</sub> camera based on gas correlation spectroscopy, *Atmos. Meas. Tech.*, 15, 1395–1414, <https://doi.org/10.5194/amt-15-1395-2022>, publisher: Copernicus GmbH, 2022.
- Last, J. A., Sun, W. M., and Witschi, H.: Ozone, NO, and NO<sub>2</sub>: oxidant air pollutants and more., *Environmental Health Perspectives*, 102, 179–184, <https://doi.org/10.1289/ehp.94102s10179>, 1994.
- 510 Lauriks, F., Jacobs, D., and Meysman, F.: CurieuzenAir: Data collection, data analysis and results, Tech. rep., Universiteit Antwerpen, 2022.
- Lohberger, F., Hönninger, G., and Platt, U.: Ground-based imaging differential optical absorption spectroscopy of atmospheric gases, *Applied Optics*, 43, 4711, <https://doi.org/10.1364/ao.43.004711>, 2004.
- Manago, N., Takara, Y., Ando, F., Noro, N., Suzuki, M., Irie, H., and Kuze, H.: Visualizing spatial distribution of atmospheric nitrogen dioxide by means of hyperspectral imaging, *Appl. Opt.*, 57, 5970–5977, <https://doi.org/ao-57-21-5970>, 2018.
- 515 Merlaud, A., Belegante, L., Constantin, D.-E., Den Hoed, M., Meier, A. C., Allaart, M., Ardelean, M., Arseni, M., Bösch, T., Brenot, H., Calcan, A., Dekemper, E., Donner, S., Dörner, S., Balanica Dragomir, M. C., Georgescu, L., Nemuc, A., Nicolae, D., Pinardi, G., Richter, A., Rosu, A., Ruhtz, T., Schönhardt, A., Schuettemeyer, D., Shaiganfar, R., Stebel, K., Tack, F., Nicolae Vâjâiac, S., Vasilescu, J., Vanhamel, J., Wagner, T., and Van Roozendael, M.: Satellite validation strategy assessments based on the AROMAT campaigns, *Atmos. Meas. Tech.*, 13, 5513–5535, <https://doi.org/10.5194/amt-13-5513-2020>, 2020.
- 520 Mettepenningen, G., Fayt, C., Tack, F., Van Doorne, C., Bogaert, P., Jacobs, L., Berkenbosch, S., Aubry, A., Desmet, F., Robert, C., De Mazière, M., and Van Roozendael, M.: UV-Vis remote sensing of atmospheric pollutants from a wind turbine platform in the North Sea: the SEMPAS project, in: EGU General Assembly 2024, Copernicus GmbH, Vienna, Austria, <https://doi.org/10.5194/egusphere-egu24-11955>, 2024.
- 525 Morrow, P. E.: Toxicological data on NO<sub>x</sub>: An overview, *Journal of Toxicology and Environmental Health*, 13, 205–227, <https://doi.org/10.1080/15287398409530494>, 1984.
- Peters, E., Ostendorf, M., Bösch, T., Seyler, A., Schönhardt, A., Schreier, S. F., Henzing, J. S., Wittrock, F., Richter, A., Vrekoussis, M., and Burrows, J. P.: Full-azimuthal imaging-DOAS observations of NO<sub>2</sub> and O<sub>4</sub> during CINDI-2, *Atmospheric Measurement Techniques*, 12, 4171–4190, <https://doi.org/10.5194/amt-12-4171-2019>, 2019.
- 530 Pettinari, P., Castelli, E., Papandrea, E., Busetto, M., Valeri, M., and Dinelli, B. M.: Towards a New MAX-DOAS Measurement Site in the Po Valley: NO<sub>2</sub> Total VCDs, *Remote Sensing*, 14, 3881, <https://doi.org/10.3390/rs14163881>, 2022.
- Platt, U. and Stutz, J.: Differential optical absorption spectroscopy, *Physics of Earth and Space Environments*, Springer Berlin Heidelberg, Berlin, [Germany] ;, ISBN 9783540757764, <https://doi.org/10.1007/978-3-540-75776-4>, includes bibliographical references at the end of each chapters and index. Description based on print version record. "With 272 Figures and 55 Tables.", 2008.
- 535 Platt, U., Lübcke, P., Kuhn, J., Bobrowski, N., Prata, F., Burton, M., and Kern, C.: Quantitative imaging of volcanic plumes - Results, needs, and future trends, *J. Volcanol. Geotherm. Res.*, 300, 7–21, <https://doi.org/10.1016/j.jvolgeores.2014.10.006>, publisher: Elsevier B.V., 2014.

- Rothman, L., Gordon, I., Babikov, Y., Barbe, A., Chris Benner, D., Bernath, P., Birk, M., Bizzocchi, L., Boudon, V., Brown, L., Campargue, A., Chance, K., Cohen, E., Coudert, L., Devi, V., Drouin, B., Fayt, A., Flaud, J.-M., Gamache, R., Harrison, J., Hartmann, J.-M., Hill, C., Hodges, J., Jacquemart, D., Jolly, A., Lamouroux, J., Le Roy, R., Li, G., Long, D., Lyulin, O., Mackie, C., Massie, S., Mikhailenko, S., Müller, H., Naumenko, O., Nikitin, A., Orphal, J., Perevalov, V., Perrin, A., Polovtseva, E., Richard, C., Smith, M., Starikova, E., Sung, K., Tashkun, S., Tennyson, J., Toon, G., Tyuterev, V., and Wagner, G.: The HITRAN2012 molecular spectroscopic database, *Journal of Quantitative Spectroscopy and Radiative Transfer*, 130, 4–50, <https://doi.org/10.1016/j.jqsrt.2013.07.002>, 2013.
- Ruiz Villena, C., Anand, J. S., Leigh, R. J., Monks, P. S., Parfitt, C. E., and Vande Hey, J. D.: Discrete-wavelength DOAS NO<sub>2</sub> slant column retrievals from OMI and TROPOMI, *Atmospheric Measurement Techniques*, 13, 1735–1756, <https://doi.org/10.5194/amt-13-1735-2020>, 2020.
- Seinfeld, J. H. and Pandis, S. N.: *Atmospheric chemistry and physics*, J. Wiley, Hoboken, N.J, 2nd ed (online-aug.) edn., ISBN 9780471720188, 2006.
- Serdyuchenko, A., Gorshelev, V., Weber, M., Chehade, W., and Burrows, J. P.: High spectral resolution ozone absorption cross-sections – Part 2: Temperature dependence, *Atmospheric Measurement Techniques*, 7, 625–636, <https://doi.org/10.5194/amt-7-625-2014>, 2014.
- Suhre, D. R., Denes, L. J., and Gupta, N.: Telecentric confocal optics for aberration correction of acousto-optic tunable filters, *Appl. Opt.*, 43, 1255, <https://doi.org/10.1364/AO.43.001255>, publisher: Optical Society of America, 2004.
- Thalman, R. and Volkamer, R.: Temperature dependent absorption cross-sections of O<sub>2</sub>–O<sub>2</sub> collision pairs between 340 and 630 nm and at atmospherically relevant pressure, *Physical Chemistry Chemical Physics*, 15, 15 371, <https://doi.org/10.1039/c3cp50968k>, 2013.
- Van Roozendael, M., Hendrick, F., Friedrich, M. M., Fayt, C., Bais, A., Beirle, S., Bösch, T., Navarro Comas, M., Friess, U., Karagkiozidis, D., Kreher, K., Merlaud, A., Pinardi, G., Piders, A., Prados-Roman, C., Puentedura, O., Reischmann, L., Richter, A., Tirpitz, J.-L., Wagner, T., Yela, M., and Ziegler, S.: Fiducial Reference Measurements for Air Quality Monitoring Using Ground-Based MAX-DOAS Instruments (FRM4DOAS), *Remote Sensing*, 16, <https://doi.org/10.3390/rs16234523>, 2024.
- Vandaele, A., Hermans, C., Simon, P., Carleer, M., Colin, R., Fally, S., Mérianne, M., Jenouvrier, A., and Coquart, B.: Measurements of the NO<sub>2</sub> absorption cross-section from 42 000 cm<sup>-1</sup> to 10 000 cm<sup>-1</sup> (238–1000 nm) at 220 K and 294 K, *Journal of Quantitative Spectroscopy and Radiative Transfer*, 59, 171–184, [https://doi.org/10.1016/s0022-4073\(97\)00168-4](https://doi.org/10.1016/s0022-4073(97)00168-4), 1998.
- Voloshinov, V. B., Yushkov, K. B., and Linde, B. B. J.: Improvement in performance of a TeO<sub>2</sub> acousto-optic imaging spectrometer, *J. Opt. A Pure Appl. Opt.*, 9, 341–347, <https://doi.org/10.1088/1464-4258/9/4/006>, 2007.
- Wagner, T., Beirle, S., and Deutschmann, T.: Three-dimensional simulation of the Ring effect in observations of scattered sun light using Monte Carlo radiative transfer models, *Atmospheric Measurement Techniques*, 2, 113–124, <https://doi.org/10.5194/amt-2-113-2009>, 2009.
- World Health Organization: WHO Global Air Quality Guidelines. Particulate matter (PM<sub>2.5</sub> and PM<sub>10</sub>), ozone, nitrogen dioxide, sulfur dioxide and carbon monoxide, WHO, Geneva, ISBN 978-92-4-003422-8, 2021.